Author's personal copy

Automated marker tracking using noisy X-ray images degraded by the treatment beam

E. Wisotzky[1,2,*], **M.F. Fast**[3], **U. Oelfke**[3,2], **S. Nill**[3]

[1] Fraunhofer Institute for Production Systems and Design Technology (IPK), Pascalstraße 8-9, 10587 Berlin, Germany
[2] German Cancer Research Center (DKFZ), Im Neuenheimer Feld 280, 69120 Heidelberg, Germany
[3] Joint Department of Physics at The Institute of Cancer Research and The Royal Marsden NHS Foundation Trust, London, SM2 5NG, UK

Received 29 January 2014; accepted 15 August 2014

Abstract

This study demonstrates the feasibility of automated marker tracking for the real-time detection of intrafractional target motion using noisy kilovoltage (kV) X-ray images degraded by the megavoltage (MV) treatment beam. The authors previously introduced the in-line imaging geometry, in which the flat-panel detector (FPD) is mounted directly underneath the treatment head of the linear accelerator. They found that the 121 kVp image quality was severely compromised by the 6 MV beam passing through the FPD at the same time. Specific MV-induced artefacts present a considerable challenge for automated marker detection algorithms. For this study, the authors developed a new imaging geometry by re-positioning the FPD and the X-ray tube. This improved the contrast-to-noise-ratio between 40% and 72% at the 1.2 mAs/image exposure setting. The increase in image quality clearly facilitates the quick and stable detection of motion with the aid of a template matching algorithm. The setup was tested with an anthropomorphic lung phantom (including an artificial lung tumour). In the tumour one or three Calypso® beacons were embedded to achieve better contrast during MV radiation. For a single beacon, image acquisition and automated marker detection typically took around 76±6 ms. The success rate was found to be highly dependent on imaging dose and gantry angle. To eliminate possible false detections, the authors implemented a training phase prior

Automatisierte Markererkennung zur Bewegungsnachführung in vom Therapiestrahl stark beeinträchtigten Röntgenbildern

Zusammenfassung

In dieser Studie wird die Detektion von intrafraktioneller Organbewegung unter Verwendung von kV-Röntgenbildern, welche durch den MV-Behandlungsstrahl stark beeinträchtigt sind, mittels automatischer Markererkennung in Echtzeit demonstriert. Die Autoren haben in einer bereits publizierten Studie die In-line-Bildgebungsgeometrie vorgestellt, in welcher der Flat-Panel-Detektor (FPD) direkt unter dem Bestrahlungskopf des Linearbeschleunigers sitzt. Dabei wurde beobachtet, dass die 121-kVp-Röntgenbilder in ihrer Qualität durch die gleichzeitigen Wechselwirkungen des 6-MV-Therapiestrahls mit dem FPD sehr eingeschränkt sind. Die MV-induzierten Bildartefakte stellen eine besondere Herausforderung für automatische Marker-Detektions-Algorithmen dar. Für diese Studie haben die Autoren eine modifizierte Bildgebungsgeometrie entwickelt: dazu wurden der FPD und die Röntgenröhre relativ zum Therapiestrahl verschoben. Dies erhöhte das Kontrast-zu-Rausch-Verhältnis zwischen 40% und 72% bei einem Setting von 1,2 mAs/Bild und ermöglichte eine schnelle und stabile Detektion der Bewegung mittels eines

* Corresponding author: Eric Wisotzky Fraunhofer Institute for Production Systems and Design Technology (IPK) Medical Technology Pascalstraße 8-9 10587 Berlin, Germany. Tel.: +493039006105

E-mail addresses: eric.wisotzky@ipk.fraunhofer.de (E. Wisotzky), simeon.nill@icr.ac.uk (S. Nill).

Author's personal copy

to treatment beam irradiation and also introduced speed limits for motion between subsequent images.

Keywords: Real-time tumour tracking, intrafractional motion, X-ray image guidance, fiducial marker, in-line geometry

template-basierten Algorithmus. Der Aufbau wurde mittels eines anthropomorphen Lungenphantoms untersucht. Ein implantierter Lungentumor wurde mit einem oder drei Calypso® Beacons ausgestattet um einen besseren Kontrast während der MV-Bestrahlung zu erhalten. Unter Verwendung eines Beacons dauerte die Bildaufnahme und automatische Markererkennung ca. 76±6 ms. Die Erfolgsrate war stark abhängig von der Bilddosis und dem Gantrywinkel. Um mögliche falsche Markererkennungen zu eliminieren, haben die Autoren eine Trainingsphase vor der MV-Bestrahlung sowie Geschwindigkeitsgrenzen für die Bewegung zwischen aufeinander folgenden Bildern implementiert.

Schlüsselwörter: Tumordetektion in Echtzeit, intrafraktionelle Bewegung, röntgenbildgestützte Nachführung, Referenzmarker, In-line-Bildgebungsgeometrie

1 Introduction

Intrafractional motion management is one of the remaining challenges in image-guided radiotherapy [1]. The traditional strategy to dosimetrically account for motion is to add safety margins around the treatment field [2]. This margin strategy considers the effect of intrafractional motion at the cost of healthy tissue irradiation [3]. Another approach, followed by our group and others [4,5], is to shrink motion related margins as much as possible and dynamically adapt the treatment field to the current position of the tumour. This technique strongly depends on constantly updated, exact knowledge of the internal tumour position. One fast and widely available imaging modality for this purpose is linac-integrated kilovoltage (kV) X-ray imaging. Different intrafractional imaging geometries were utilised in previous studies: e.g. the orthogonal [6], the stereoscopic [7] and the in-line [8] geometry.

The original in-line geometry [9], in which the kV imaging and megavoltage (MV) treatment beam are perfectly aligned (config. I, Fig. 1 (a)), is not suitable for tumour tracking during MV irradiation, because of the overlap of kV and MV field on the flat-panel detector (FPD). Fast et al [8] shifted the X-ray source 13 cm toward the gantry and thus effectively tilted the kV beam by 5.4° to create a geometric separation of MV and kV fields suitable for intrafractional imaging (config. II, Fig. 1 (a)). The system is capable of tracking most target motions perpendicular to the treatment beam, the direction that usually features steep dose gradients. In principle, it is also possible to monitor the shape of the treatment field using this geometry, a feature that could provide useful additional information when the treatment is dynamically adapted. In their approach, however, poor kV image quality and MV-induced artefacts still posed a considerable challenge for automated tumour detection. Major artefacts caused by the treatment beam are an increase of noise through scatter within the detector, the multi-leaf-collimator (MLC) leakage and MV stripe artefacts. The latter artefact is caused by the pulsed nature of the MV beam and the non-synchronous FPD readout [10].

In this study we have enhanced the modified in-line imaging geometry [8] further for better kV image quality and reduced MV-induced artefacts. This was achieved by repositioning the FPD and kV tube with respect to the treatment beam (config. III, Fig. 1 (a)). Importantly, we also rotated the FPD 90° about the treatment beam axis to improve its read-out behaviour. A stripe reduction algorithm was implemented to mitigate the effect of the MV stripes.

The aim of this study was to develop and improve an automated method for real-time detection of respiratory target motion during treatment with the aid of metallic markers based on X-ray images acquired in the new in-line geometry. The real-time requirement is crucial for performing the motion compensation adequately and yielding the required dosimetric effect [11]. The accuracy of the detection algorithm is equally important, and we established a training phase prior to MV irradiation to exclude incorrect marker positions during treatment. To gauge the suitability of the new imaging geometry for target localisation, we experimentally simulated respiratory tumour motion by using an in-house built anthropomorphic lung phantom with implanted Calypso® (Varian Medical Systems, Inc., Palo Alto, CA, USA) beacons as markers. Simple sinusoidal trajectories that simulate regular respiration were complemented by more irregular breathing patterns that mimic the effect of coughing. Following the suggestions by Harris et al [12], we implemented a template matching algorithm based on normalised cross-correlation to automatically detect the marker motion. Previous studies [13–15] have demonstrated that automated marker detection with grey-value templates can yield excellent results when

Author's personal copy

using high quality X-ray images undisturbed by MV irradiation. In this study, this knowledge will be extended for the kind of noisy MV-degraded X-ray images acquired with the in-line geometry.

2 Materials & Methods

2.1 Experimental setup

The experimental setup, see Fig. 1 (a), already described by Fast et al [8] is further adapted to improve the X-ray image quality. The setup comprises of a Siemens ARTISTE research linac with an additional amorphous silicon FPD mounted 61.5 cm underneath the MV source. Compared to our previous setup (config. II), the FPD is rotated by 90° about the *z*-axis and shifted by -7.5 cm in the *y* direction. The Siemens OPTITOP 150/40/80 HC-100 diagnostic X-ray tube is installed on a retractable stage opposite to the treatment head. For this study, the X-ray tube is retracted toward the gantry by approximately 36.5 cm (*y* direction) and rotated by 15° about the *x*-axis. This rotation was previously impossible due to a mechanical limitation of the retractable stage. In addition the jaws of the X-ray collimator were applied asymmetrically in such a way that the positive *y* direction was more collimated than the negative *y* direction. This resulted in an larger effective tilt of approximately 20° for the isocenter kV ray. This yields a relative separation of 12.4 cm between the kV image and MV treatment field centres on the FPD. The kV field-of-view was narrowed to approximately 4×6 cm^2 at the isocenter to avoid unnecessary imaging dose. The source-to-isocenter distance and the source-to-detector distance for the isocenter kV ray are 106.3 cm and 154.2 cm respectively.

Resulting from the modified FPD position and the 90° rotation, the MV treatment field and the non-coplanar kV image are displayed on different subpanels of the FPD (Fig. 1 (b)). The FPD is an XRD 1640 AN9-ES X-ray radiation image detector from PerkinElmer (Fremont, CA, USA). As in our previous studies, the 1 mm Cu built-up plate was removed to avoid filtration of the kV imaging beam and reduce backscatter (originating from the MV treatment beam) into the adjacent phosphor layer [16]. The active area of the detector is about 40.96×40.96 cm^2 (matrix size: 1024×1024 pixels, pixel size: 0.4×0.4 mm^2). Due to the design of the FPD (the XRD 1640 FPD is divided into two parts, each of them consisting of eight 128×512 pixel read-out groups corresponding to a single amplifier chip), the active area is split into two subpanels with independent read-out electronics [17,10]. In this study, the 3 mm Al backplate of the FPD is also removed to decrease absorption and scattering of the MV beam [16].

2.2 Image acquisition

For image acquisition the following settings were employed: a 121 kVp energy setting, a detector gain setting of 8 pF, the fastest available readout time (t_{acq} = 66.6 ms), and an overall frame rate of 14.3 Hz corresponding to a new frame trigger signal every 70 ms. The frame grabber and associated C++ library from PerkinElmer were used for direct frame

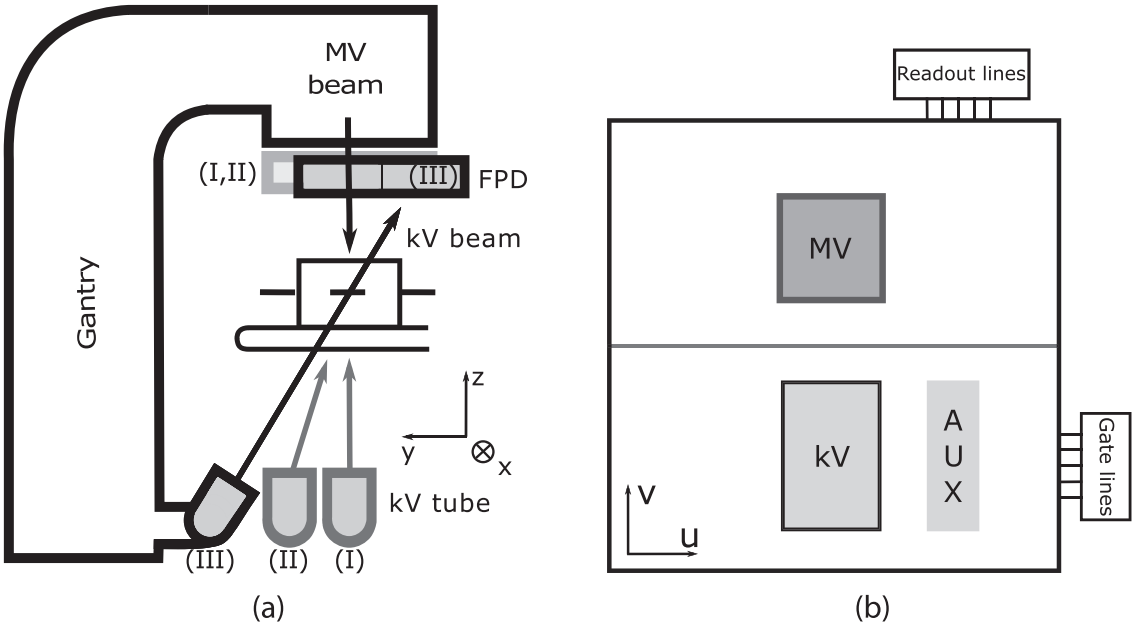

Figure 1. (a) Evolution from the original in-line geometry (config. I, [9]), to the modified in-line geometry (config. II, [8]), and finally the new in-line geometry (config. III). Side view of the experimental setup and orientation of the room coordinates. (b) Schematic front view of the detector where the subpanel border (grey horizontal line) is located between non-coplanar kV image and MV field. The auxiliary region is used to identify the MV stripe artefacts oriented along the gate line direction (section 2.3).

Author's personal copy

access. The image acquisition and marker detection workflow was implemented in C++:

1. Acquire image pair: kV-free image N & kV image $N+1$ (MV treatment beam constantly on).
2. Subtract MV-only image N from kV image $N+1$.
3. Perform image corrections: gain, dead-pixel and MV stripe corrections.
4. Perform marker detection using template matching.
5. Back-project marker positions to room coordinates.

The stripe correction algorithm (iii) and the template matching algorithm (iv) are described in detail in sections 2.3 and 2.5. The other steps are described by Fast et al [8]. Compared to our previous implementation, we moved step (iv) from Matlab® (The MathWorks, Inc., Natick, MA, USA) to C++ which reduces computational costs. To speed up image processing, Open Multi-Processing (OpenMP), a shared memory multiprocessing platform [18] was used in our software framework. Additionally, steps (iv) and (v) were multi-threaded (three threads). Thus only every third image was handled by the same thread which is a built-in safety buffer for latency outliers.

2.3 MV stripe reduction

Detector rows that are read out during an MV pulse display a systematically higher signal than other rows [10]. Because of the non-synchronous FPD readout, the stripes are in different rows for every frame and simply subtracting subsequent images does not remove the stripes. The separation of the kV and MV fields onto different subpanels reduces the stripe amplitudes in the kV image because of the separated read-out electronics (Fig. 2).

Residual stripe signal was further reduced by determining the median stripe amplitude for each detector row from a neighbouring kV-free auxiliary region (see Fig. 1 (b)) and subtracting it from the corresponding row in the kV image.

2.4 Dose and image quality

As with any X-ray imaging system, the choice of exposure setting is a compromise between imaging dose to the patient and image quality. We measured the dose by using a simple $30\times30\times20$ cm^3 RW3 phantom and a PTW Semiflex 0.125 cm^3 ionization chamber. To estimate the dosimetric implications of our system we measured doses for 0.6 mAs, 1.2 mAs, 2.0 mAs and a 2.5 mAs per x-ray projection. The source-to-surface distance was 90 cm. Central doses were measured at 10 cm depth and surface doses at 2 cm depth to account for the build-up effect.

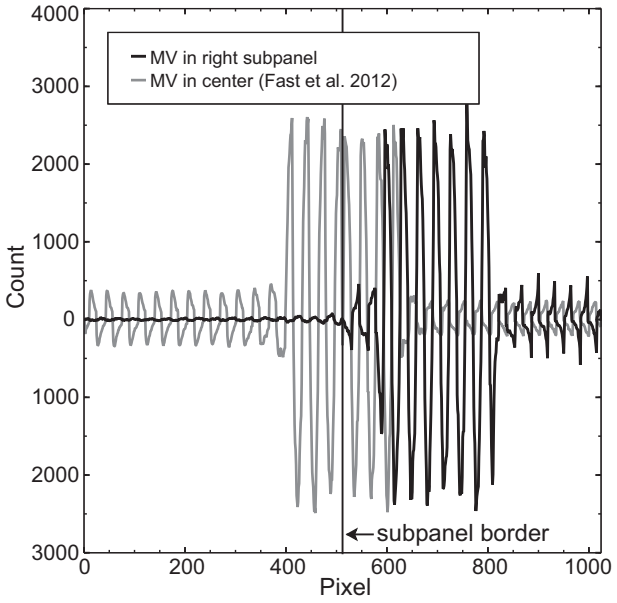

Figure 2. Line profile through a difference image (two subsequent kV-free frames, MV constantly on) highlighting the stripe artefacts. When the primary MV field is contained within one subpanel, the stripes on the other subpanel are greatly reduced in amplitude.

In order to quantify the overall image quality and thus the efficacy of the stripe reduction algorithm, we measured the commonly used contrast-to-noise ratio (CNR) metric:

$$CNR = \frac{|\overline{S_{ROI1}} - \overline{S_{ROI2}}|}{\sqrt{\sigma^2_{ROI1} + \sigma^2_{ROI2}}}, \quad (1)$$

with $\overline{S}$ as the mean signal intensity of a circular (radius: 50 pixels) region-of-interest (ROI) and the standard deviation σ_{ROI} of the signal intensity within a ROI. Materials of different relative electronic density were used. Measured with respect to nearly water-equivalent RW3 (1.012), these were: lung (0.28), adipose tissue (0.9), spongy bone (1.11) and cortical bone (1.71). The disk-shaped contrast material with 1 cm thickness and a diameter of 3 cm was sandwiched by 10 cm of RW3 on each side. CNR measurements were compared with and without an 8×8 cm^2 300 MU/min 6 MV radiation field turned on. The experiments were performed at 121 kVp at a low (1.2 mAs/projection) and a high (2.5 mAs/projection) imaging dose setting. We performed the dose and image quality measurements at the 0° gantry angle.

2.5 Motion tracking

2.5.1 Automated marker detection

To identify the markers in the kV images we employed a grey-value template matching algorithm [12]. The algorithm uses normalised cross-correlation (NCC) to compare marker

Author's personal copy

template and acquired X-ray image. The cross-correlation measures the similarity between both images. To reduce the impact of offset or brightness variations on the correlation values, the image as well as the template have to be normalised. The NCC term sums over the number of pixel N of the selected ROI,

$$NCC = \sum_{i=1}^{N} \frac{(f_i' - \overline{f'})(t_i - \bar{t})}{\sigma_{f'}\sigma_t}, \quad (2)$$

using $\overline{f'}$ and $\bar{t}$ as the mean values and $\sigma_{f'}$ and σ_t as the standard deviation of image f' and template t.

For automated marker detection, the template is moved across the entire ROI and the NCC value is calculated for each pixel. All pixels within a distance of half the template size to the ROI border are boundary pixels and are therefore not assigned with an NCC value. Our template matching procedure also depends on the number of expected markers. For a single marker, the template is moved over the ROI and the largest matching value m_{NCC} gives a potential marker position i. To eliminate the possibility of a mismatch caused by poor contrast, an empirical threshold $r = 0.85$ is given and m_{NCC} at the position i must exceed this threshold ('max. correlation'). The threshold value of r was chosen to reflect a good compromise between a safe match and the uncertainty caused by noise. In addition, the median of the neighbouring pixel of i has to also exceed a threshold $r' = 0.8$. This second correlation value is called 'med. correlation'. This condition is included to eliminate the possibility of random matches caused by noise. For the correct template position, a shift of one pixel in every direction should not result in a large reduction of m_{NCC}. If both conditions are fulfilled, the detected position i will be back-projected into the isocentre plane using a pre-calculated projection matrix $\boldsymbol{P}$ [8]. For every image the 61×61 pixel ROI is centred around the last detected marker position and thus moves along with the marker movement. If the detection fails in one image the ROI size will be increased for the next image by 10 pixels in every direction. This increase is assumed to account for the maximum marker shift caused by regular breathing.

2.5.2 Detection of three markers

Tracking of multiple markers is often desirable, since the centre-of-gravity motion of a tumour is only fully described by three or more markers implanted around the tumour volume. We found that simply extending our single marker strategy to multiple markers by repeatingly calculating NCC values for each individual template over the entire ROI was computationally too expensive. Therefore we identified only the first marker position i by calculating NCC values for the entire image (160×220 pixels) and then used prior geometric knowledge (cf. section 2.5.3) about the relative distances of the markers.

NCC values for the second marker were only calculated for image pixels on a circle around the first marker position with a radius equal to the distance d_{ij} between the first and the second marker. To accommodate for small variations between the real and the assumed marker distance, the largest matching value m_{NCC} of the second marker must only exceed $r' = 0.8$. The position of this pixel is referred to as preliminary position j' of the second marker. The area spanned by ± 5 pixels around j' is then searched for an m_{NCC} value exceeding r to identify the true position of the second marker j and eliminate the uncertainty arising from d_{ij}.

Once the second marker is correctly identified, only two positions k are possible for the third marker (the intersections of the circles with radius d_{ik} and d_{jk}). When the NCC value of a single pixel from the 15×15 pixel neighbourhoods of these candidate positions exceeded $r = 0.85$, we assumed the third marker to be correctly identified. The larger size of the neighbourhood region reflects the uncertainty in d_{ik} as well as d_{jk}.

2.5.3 Template creation

In order to create a grey-value template, 3-6 images of the phantom were acquired prior to treatment beam irradiation. We then manually identified the approximate marker position in each image. A region cropped around the marker in the first image was then used as a template to calculate NCC values at the approximate marker position (±9 pixels) of the second image. The position with the highest match m_{NCC} is assumed to be the centre of the first template iteration. The regions cropped from the first and second image are then averaged to calculate the first iteration of the template. The quality of the created template is analysed by looking at the standard deviation of the two input images. For the next images the same procedure is iterated and the template is an average of the best matches of all 3-6 images. The mostly non-square templates varied in size between 7-21×9-21 pixels depending on the marker and gantry angle. For multiple markers, the distances d_{ij}, d_{ik} and d_{jk} between markers were also identified. In future, the grey-value templates [15] and the geometric information about the 3D marker positions should be automatically extracted from planning CT, CBCT or digitally reconstructed radiograph (DRR) data for every treatment fraction.

2.5.4 Region and maximum-shift filters

For some x-ray images, random noise fluctuations will lead to erroneously identified marker positions despite the two thresholds r and r' described in section 2.5.1. Therefore, two additional constraints were implemented: the region filter and the maximum-shift filter.

The region filter continuously calculates probable marker locations by analysing the history of previous marker positions. For multiple markers, the centre-of-gravity positions are analysed. An ellipse is fitted to the previous positions and if the next detected position is not within this ellipse it is

Author's personal copy

probably incorrect (Fig. 3). Consequently, the treatment beam was only engaged after the initial training phase was completed. To avoid a skewing of the ellipse, all evenly-sampled data points from the previous respiratory cycle(s) should be analysed. In this study, we have chosen to always take the two latest respiratory cycles c_s into account. The number of required input positions/images n_t is calculated as follows:

$$n_t = \frac{2c_s}{R \cdot T}. \tag{3}$$

Assuming $c_s = 4500$ ms, a frame trigger time of $T = 70$ ms, and the fact that every second frame is a kV image ($R = 2$), this amounts to approximately 65 kV images. By continuously updating the ellipse with the last n_t positions, we ensure that systematic drifts or slow changes in breathing period are captured by our region filter. In cases with more complex tumour motion, the ellipse criterion could be replaced by a probability density function [19].

Additionally, a limit on the maximum shift in marker (or centre-of-gravity) position between subsequent frames was imposed. This limit can be derived from prior knowledge about the respiration of the patient. For our phantom experiments, $v = 45$ mm/s was implemented as limit. If the observed shift is outside of the calculated maximum range, the new marker position is assumed to be incorrect (or it may reflect an extraordinary event such as coughing). The shift s in mm between two subsequent frames is calculated as follows:

$$s = v \cdot \Delta T. \tag{4}$$

Here, v is the maximum marker speed derived from prior knowledge and ΔT is the time difference between the current image and the last image with a successfully identified marker.

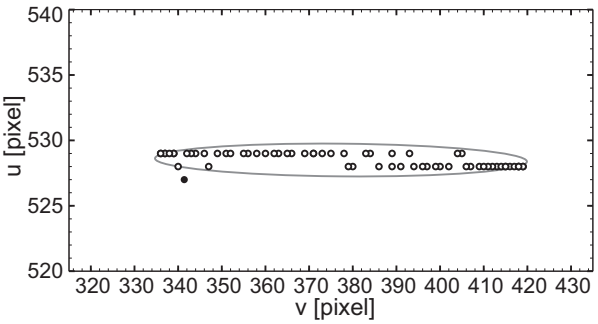

Figure 3. The grey ellipse is plotted around detected marker positions (on the FPD) from the last two breathing cycles. The major axis has a length of 16.9 mm and the minor axis has a length of 1 mm. The filled black dot represents an incorrectly identified marker position which is excluded by the region filter.

2.5.5 *Latency*

The total system latency t_{sys} can be split into different components:

$$t_{sys} = t_{acq} + t_{pre} + t_{\mathrm{det}} + t_{post}. \tag{5}$$

The main contributor to t_{sys} is the image acquisition time of $t_{acq} = 66.6$ ms. This time is constant for all images (cf. section 2.2). Image pre-processing (t_{pre}) encompasses all computations that are necessary to prepare the image for template matching (t_{det}). Post-processing (t_{post}) includes the application of the position filters. The computational run time is therefore defined as:

$$t_{alg} = t_{sys} - t_{acq}. \tag{6}$$

Ideally, t_{alg} should be well below t_{acq} such that the marker search is finished before the next frame is acquired. Thus, our real-time requirement amounts to $2 \times t_{acq} = 133.2$ ms. The different latencies were recorded in log-files during the experiments for analysis.

2.6 Lung phantom

To simulate lung tumour motion we employed a DKFZ-developed thorax phantom which is modelled on a patient CT scan [20]. The phantom contains two lung lobes surrounded by water-equivalent material and is mounted on a carriage to simulate periodic movements in y-direction. The phantom was slightly widened in superior-inferior (SI) direction to account for the tilted imaging beam in the new in-line geometry. It now consists of 21 slices of 1 cm thickness. The height (anterior-posterior, AP) of the phantom is approximately 25 cm and the width (left-right, LR) is around 30 cm. Slices were manufactured from water-equivalent RW3 and lung-equivalent obomodulan type 300. The lung material has a density of approximately 0.3 g/cm^3. A tumour, also consisting of RW3, was embedded in the right lobe of the lung. One or three markers were implanted into the tumour at different orientations with respect to the imager. As the in-house developed phantom was set up for use with the Calypso® beacons for a previous study, we opted to keep the same configuration. Each beacon (length: 8.5 mm; diameter: 1.85 mm) consist of a ferrite core (Z=26), a copper coil (Z=29) and glass [21].

The tumour extends 3 cm in SI, 5.1 cm in AP and 3.1 cm in LR. It is important to note that the radiological length along the central kV ray through the phantom is shorter at gantry angle 90° than at gantry angle 0° due to the internal design of the phantom. The phantom is mounted on tracks and can be moved with the aid of an adjacent motor. The movement

Author's personal copy

of the tumour is characterised by the tumour position $s(t)$ as a periodic, but asymmetric function of time [22]:

$$s(t) = s_0 - A\cos^2(\frac{\pi t}{\tau}). \quad (7)$$

The amplitude of the breathing cycle is $A = 2.5$ cm. The tumour position at exhalation is s_0, and $s_0 - A$ at inhalation. The period of the breathing cycle was chosen to be $\tau = 4.5$ s, corresponding to a respiratory rate of approximately 13 per minute. The movement is carried out in y direction, the SI direction. Coughing was simulated by adding an additional asymmetric modulation to $s(t)$.

All lung phantom measurements were performed either at 0° or at 90° gantry angle. At 90° gantry angle, the lowest possible dose setting (0.6 mAs) was used and at 0° gantry angle, measurements with 1.2 mAs, 1.6 mAs, 1.8 mAs, 2.0 mAs and 2.5 mAs were taken.

2.7 Validation of marker detection performance

To quantify the detection results, the quantities *success rate* and *accuracy* were used. The success rate measures the number of frames assigned with a marker position (correct or incorrect) as a fraction of the total number of frames. The accuracy indicates how many marker positions were correctly identified (inspected by a human observer).

3 Results

3.1 MV stripe artefacts

We first quantified the improvement of our new imaging setup in terms of MV stripe artefact reduction. We observed that the intensity of the stripes varied in u-direction for the previous imaging in-line geometry (config. II, Fig. 1). The mean stripe intensity at a distance of 2.5 cm from the MV field edge was 124.5 ± 33.2 and at a distance of 10 cm the amplitude was 50.3 ± 13.2 for a 14×14 cm^2 treatment field. For the imaging setup used in this study (config. III), the residual stripe signal is orientated along the v-direction and constant across the kV ROI (43.3 ± 12.5). In Table 1, the stripe signal level for the new and the previous setup is presented for different MV field sizes and shapes. It can be observed that stripe signal generally drops for smaller MV fields and that the difference between old and new setup narrows.

Table 1
Residual MV stripe signal for the new rotated and shifted detector setup (config. III, Fig. 1 (a)) and the previous setup (config. II). The round MV field had a radius of 1.5 cm.

MV field [cm^2]	config. III	config. II (at 2.5 cm)	config. II (at 10 cm)
14×14	43.3 ± 12.5	124.5 ± 33.2	50.3 ± 13.2
8×8	26.0 ± 8.4	57.0 ± 14.9	29.4 ± 9.4
round	22.1 ± 7.9	25.8 ± 10.0	24.6 ± 9.8

3.2 Image quality and imaging dose

When comparing images corrected with the MV stripe reduction algorithm (section 2.3) with uncorrected images, the reduction in noise and increases in contrast become obvious. Fig. 4 (a) & (b) shows that the presence of MV irradiation is not easily noticeable in the corrected images. A small MV-induced signal increase of 9.7 ± 14.5 counts is measured for the kV ROI. An uncorrected image (Fig. 4 (c)) is shown for reference. Even stronger degradation of kV image quality was observed with our previous imaging configuration (cf. figure 3 from Fast et al [8]).

Fig. 5 (a) shows how the stripe reduction algorithm improves the CNR for all material for both dose settings. For cortical bone (density: 1.71), for example, the CNR increased by 40.3% for the low dose setting and by 31.6% for the high dose setting. For lower density spongy bone (density: 1.11) the CNR increase was 48.8% at the low dose setting. Except for adipose tissue, the CNR increase at a certain dose setting was similar for each tissue type. Compared with the kV-only images, the difference in CNR is halved by the stripe reduction algorithm.

We measured the average dose per projection for a central and surface position of the phantom (Fig. 5 (b)). The fitted curve is a linear function $y = a \cdot x$ with parameter $a = 0.025$ Gy/As for the central dose measurement and $a = 0.093$ Gy/As for the surface dose measurement. If the system would operate at its current kV imaging frequency of 7.14 Hz using a low-dose protocol of 0.6 mAs, the surface imaging dose would reach 1 Gy after approximately 41.5 min and the central imaging dose would reach 1 Gy after approximately 158.7 min.

3.3 Detection latency

The total system latency of image acquisition and marker detection (section 2.5.5) with MV irradiation was measured for all exposure settings to be approximately 75.7 ± 5.7 ms for a single marker detection at gantry angle 0° with t_{pre} amounting to 2.7 ms, t_{det} to 1.1 ms and t_{post} to 3.3 ms. Without MV irradiation the total system latency was marginaly reduced to 73.2 ± 2.9 ms. The presence of MV irradiation (or in fact the gantry angle) therefore made hardly any difference in terms of the total system latency. The combined latency, eq. (6), for image pre-processing t_{pre}, template matching t_{det} and image post-processing t_{post} is presented in Figure 6.

It is noticeable that the variability of the latency decreases with higher dose settings. The high number of latency outliers at the lowest does setting are caused by lower contrast. For some frames more than one candidate location needs to be checked against the preset empirical thresholds which adds to the computation time.

Author's personal copy

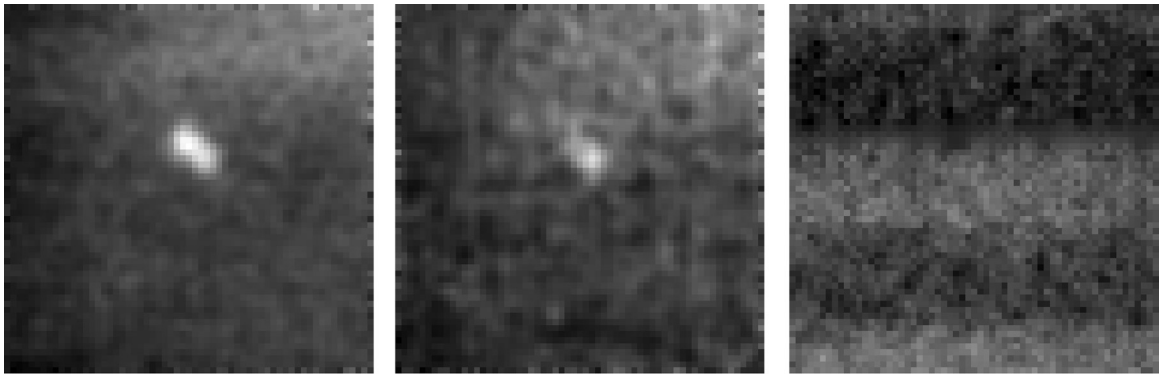

Figure 4. (a) Reference image without MV irradiation. (b) Stripe reduction algorithm applied to image with MV irradiation present. (c) Image with stripe correction turned off (without marker in phantom). All images were acquired with the same exposure setting (2.5 mAs).

For the detection of three markers the latency of the algorithm t_{alg} increases to 15.35±6.81 ms. This increase compared to the single marker detection is mainly due to an increase in t_{det} caused by the larger ROI size and the additional calculation steps necessary to find three markers (section 2.5.2). The latencies for pre-processing and post-processing stay constant compared to the single marker detection. We measured t_{alg} values ranging from 8.8 ms to 41.8 ms. Curiously, the long latency outliers were only observed in one of the three program threads and only during multiple marker acquisition. Since the frames with latency outliers did not visibly differ from other frames of the acquisition, we attribute this behaviour to interference from an additional CPU load scheduled by the operating system and other applications.

3.4 Marker detection

3.4.1 Single marker detection

As expected, the accuracy and success rate (section 2.7) of marker detection increased with imaging dose due to improved contrast. In Figure 7 (a) the normalised cross-correlation values are plotted for the 0.6 mAs low dose setting acquired at gantry 90°. Although max. correlation as well as med. correlation values (section 2.5.1) drop significantly in the presence of MV irradiation, they are both well above 0.8 for all frames. For this setting we recored a success rate of 100% based on 405 frames and also an accuracy of 100%. No improvement could thus be achieved by using higher doses.

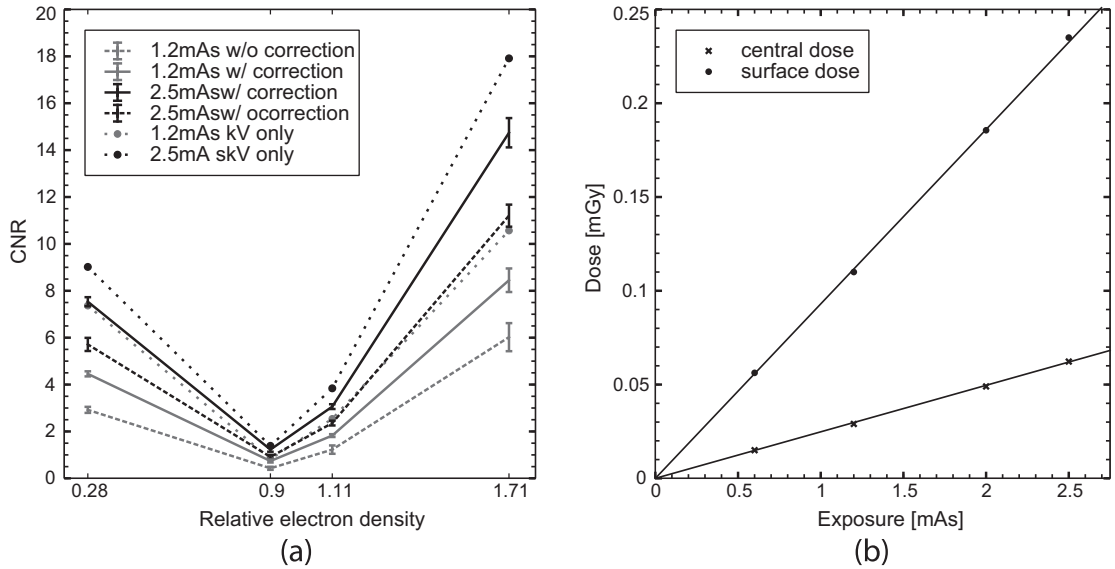

Figure 5. (a) The CNR values during MV radiation with and without MV stripe correction and without MV radiation for materials with different electron density. For the kV-only measurements the errors are too small to be shown. (b) The measured dose at certain exposure settings and the associated fitted dose curve.

Author's personal copy

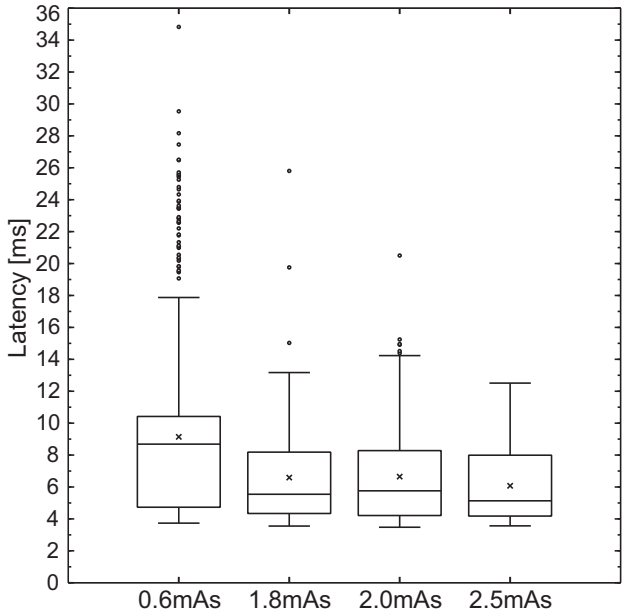

Figure 6. The latency of the detection algorithm t_{alg} (eq. (6)) during MV irradiation. The gantry position is 0°, except for 0.6 mAs (here gantry angle: 90°).

Due to the internal phantom design, marker detection at gantry angle 0° was more challenging. Figure 7 (b) demonstrates that the correlation value clearly increases with imaging dose, especially in the presence of MV irradiation. For the 2.5 mAs high dose setting, the success rate was 97.2% based on 245 frames. In 1.2% of all frames no marker could be found by the algorithm and in 1.6% of all frames an incorrect marker position was initially located, but all positions were excluded by the region and/or maximum-shift filter. Therefore an accuracy of 100% could be achieved. For 2 mAs (368 frames) the success rate dropped to 66% and for 1.8 mAs (331 frames) it was 44.4%. The accuracy, however, only decreased to 99.5% and 98.8% respectively, again demonstrating the positive impact of our position filters. Without MV irradiation, the 1.2 mAs exposure setting achieved an accuracy of 99.6% which is more than adequate for the training phase (two respiratory cycles) necessary to initiate the region filter (section 2.5.4).

To challenge our region and maximum-shift filters with extraordinary respiratory events, we simulated coughing by adding sudden and rapid shifts to the phantom trajectory. Now markers could either move entirely out of the initial ROI, or be excluded by region and/or maximum-shift filter. We observed that depending on the speed of the breathing cycle, our algorithm was able to recover the right marker position within 1-2 images by increasing the ROI size and relaxing the maximum-shift constraint. Only when the breathing period was accelerated to an unrealistic 2 s, did the algorithm need 8-10 frames to recover.

3.4.2 *Multiple marker detection*

When detecting three markers, the total success rate/accuracy is usually lower than for a single marker detection since the individual success rates/accuracies of the three markers are interdependent. At gantry angle 90° the success rate was 98.6% based on 513 frames using the 0.6 mAs low dose setting. The accuracy of finding the first marker is 100%, two markers 99.6% and all three markers 99.2%. Here, the individual accuracy of finding the third marker was also 99.6%. As for the single marker detection, the results get slightly worse at gantry angle 0° using the

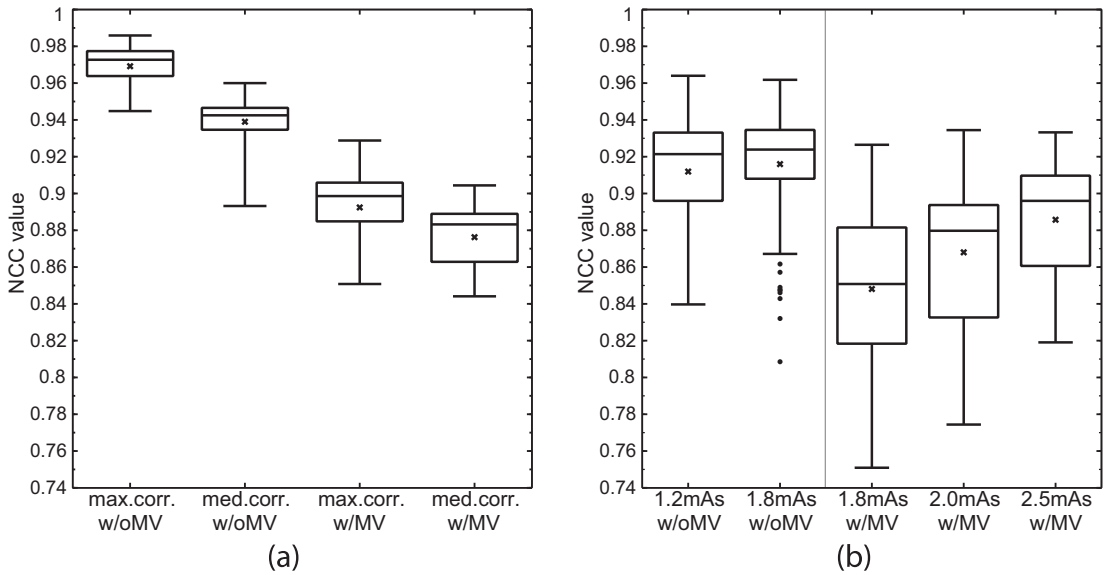

Figure 7. (a) A significant decrease of the NCC value can be observed in the presence of MV irradiation (90° gantry angle and 0.6 mAs exposure). (b) The NCC value increases with exposure and becomes more stable (0° gantry angle).

Author's personal copy

2.5 mAs high dose setting. The success rate dropped to 95.1% based on 529 frames. The accuracy of finding the first marker was 96.8%. For the second marker the accuracy was 99.8%, but the success rate was only 89.5%. This success rate decrease for the second marker results from the potential errors in the analysed position and the template quality. The success rate of the third marker was 89.2% and its accuracy was 99.2%. Therefore in 73.5% of the 529 images all three markers were correctly detected.

4 Discussion

In this study, we have experimentally demonstrated the feasibility of our new in-line imaging geometry as a monitoring device for intrafractional respiratory motion. The proposed geometry is a concept evolved from previous work by Fast et al [8]. In contrast to orthogonal kV imaging systems, our system is able to detect most tumour movements orthogonal to the treatment beam, the plane which usually features steep dose gradients [23]. Additionally, the shape of the MV field can be monitored with the same detector which is potentially beneficial for MLC-tracking. Compared to MV imaging approaches [24,25], the imaging field of view is almost independent from the treatment field.

Since MV and kV beams are impinging on the same imaging detector, certain MV-induced artefacts, most prominently the MV stripe artefact, must be considered. We could demonstrate a stripe reduction algorithm which narrows the contrast gap between kV images acquired during MV irradiation and kV-only images by 50%. In comparison to Fast et al [8] the CNR improves by up to 72.2% as a result of setup improvements and the stripe reduction algorithm. The intensity of the stripes in the entire kV ROI is homogenised and strongly reduced compared to the previous setup, e.g. by around 60% for the 14×14 cm^2 treatment field. This improvement is due to the separation of kV and MV fields into two (electronically independent) subpanels of the flat-panel detector. In a separate study, Fast et al [16] showed that the image quality can be further improved by optimising the flat-panel detector for use in the in-line geometry

Unfortunately, the visual impression of the achievable kV image quality also demonstrated to us that the improved contrast is, despite the improvements, still not good enough to attempt tracking of anatomical features i.e. marker-less tracking. This is clearly due to the fact that we had to use a coarse detector gain setting of 8 pF to avoid detector saturation (by the MV beam) instead of the usual 0.5 or 1 pF. With the aid of Calypso® beacons as markers, however, the improved contrast can yield an excellent tracking accuracy. Our anthropomorphic lung phantom study has shown that for both analysed gantry angles, success rates of >97.2% with accuracies of 98.8% or higher are possible. This compares well with other marker-based tracking results [12,26] and is better than the published results for marker-less tracking [24]. Switching from Calypso® beacons (Z=26/29) to solid gold markers (Z=79) should increase x-ray absorption within the markers due to the strong Z-dependence of the photoelectric effect. This increased absorption should equalize the effect of lower contrast caused by the smaller gold marker dimensions and altogether further improve contrast. At gantry angle 90°, we were able to detect the marker in every frame at the lowest dose setting (0.6 mAs). Here, NCC values were well above 0.8 which indicates an excellent correlation. Fail-safe mechanisms such as the region filter and the maximum-shift filter proved useful in keeping the number of false-positive detections low for acquisitions at gantry angle 0°. Even with simulated coughing our algorithm was able to recover the correct marker position within 1-2 frames. For three markers, the correlation values differ for each marker, but were of the same order of magnitude as for the single marker detection. Ideally the success rate and accuracy would be the same for all three markers. In reality both quantities differ from marker to marker, because the templates quality and size is not always identical. In our algorithm the search space for the second and third marker is also dependent on the position of the first marker which can introduce additional errors. One clear limitation of our current algorithm for multiple marker detection, to be addressed in future studies, is the effect of target rotations and marker migration on the tracking accuracy and latency.

The total system latency was usually much better than $t_{sys} \approx 85$ ms for a single marker detection and better than $t_{sys} \approx 95$ ms for three markers. This is clearly faster than our real-time requirement of 133.2 ms, derived from the maximum imaging frequency. It is also much faster than the >100 ms reported by Poulsen et al [27] who did not have direct image access. Image processing times reported by Cho et al [28] were considerably slower at ~50 ms. Compared to Fast et al [8] the latency of a single marker detection decreased by about 10 ms despite the greatly increased complexity of the marker detection algorithm (NCC instead of simple thresholding; position filters). To find multiple markers in one image, more detection steps are necessary and this is clearly reflected in the latency. Nonetheless, the latency for three markers was also well below our limit of 133.2 ms.

As with any X-ray based imaging system, there is a compromise between high image quality and low patient exposure. For the surface dose, we achieved a dose rate of 4.185 cGy/min using our lowest exposure setting of 0.6 mAs/projection, which is comparable to previously published dose values [29,30]. Clearly, the necessary imaging dose per projection depends on the patient size and gantry angle. To limit the imaging dose to the patient, we demonstrated that the imaging frequency can be safely reduced by correlating internal motion to external motion measured by an additional exposure-free monitoring system [31]. Ng et al [32] have recently reported that a total dose of 2-10 mSv can be sufficient to monitor (slower) prostate motion at an imaging frequency of 1 Hz during the entire treatment. Reducing the X-ray exposure not only during treatment but also for the training phase of the region filter (two respiratory cycles before treatment), would

Author's personal copy

be another important dose-saving mechanism, but was not available for this study due to technical limitations of the system.

Achieving reliable tumour tracking is harder to achieve without high-contrast markers as aid. Furtado et al [33] have reported on marker-less tracking using high-quality X-ray images and DRRs as templates. Avoiding the invasive procedure of implanting markers into the patient is of course desirable, but it might also come at the cost of reduced geometric accuracy. The sub-mm accuracy of our system [8] compares well with the root-mean-square error of 2.1 mm reported by Furtado et al [33].

Given the improvements in image quality and marker tracking performance reported in this study, and the additional gains achievable by using a customised X-ray detector [16], we believe that the new in-line geometry is a powerful tool for intrafractional imaging that should be considered for testing in a clinical environment next.

Acknowledgement

Research presented in this paper was conducted at the German Cancer Research Center (DKFZ). Thanks to Gernot Echner and Armin Runz (both DKFZ) for support of the experimental setup.

References

[1] Keall P, Mageras G, Balter J, et al. The management of respiratory motion in radiation oncology report of AAPM task group 76. Medical Physics 2006;33:3874.
[2] ICRU, Report 62, Prescribing, Recording and Reporting Photon Beam Therapy (Supplement to ICRU Report 50).
[3] Korreman S, Rasch C, McNair H, Verellen D, Oelfke U, Maingon P, Mijnheer B, Khoo V, et al. The European society of therapeutic radiology and oncology-european institute of radiotherapy (estro-eir) report on 3d ct-based in-room image guidance systems: A practical and technical review and guide. Radiotherapy and Oncology 2010;94(2):129.
[4] Keall P, Kini V, Vedam S, Mohan R. Motion adaptive x-ray therapy: A feasibility study. Physics in Medicine and Biology 2001;46(1):1.
[5] Tacke M, Nill S, Oelfke U. Real-time tracking of tumor motions and deformations along the leaf travel direction with the aid of a synchronized dynamic MLC leaf sequencer. Physics in medicine and biology 2007;52(22):N505.
[6] Poulsen P, Cho B, Sawant A, et al. Dynamic MLC tracking of moving targets with a single KV imager for 3d conformal and IMRT treatments. Acta Oncologica 2010;49(7):1092–100.
[7] Berbeco R, Jiang S, Sharp G, et al. Integrated radiotherapy imaging system (IRIS): design considerations of tumour tracking with linac gantry-mounted diagnostic X-ray systems with flat-panel detectors. Physics in medicine and biology 2004;49(2):243.
[8] Fast MF, Krauss A, Oelfke U, et al. Position detection accuracy of a novel linac-mounted intrafractional X-ray imaging system. Medical Physics 2012;39(1):109.
[9] Oelfke U, Tücking T, Nill S, Seeber A, Hesse B, Huber P, Thilmann C. Linac-integrated kV-cone beam CT: Technical features and first applications. Medical Dosimetry 2006;31(1):62–70.
[10] Mooslechner M, Mitterlechner B, Weichenberger H, Huber S, Sedlmayer F, Deutschmann H. Analysis of a free-running synchronization artifact correction for MV-imaging with aSi:H flat panels. Physics in medicine and biology 2013;40(3):1906.
[11] Krauss A, Nill S, Tacke M, Oelfke U. Electromagnetic real-time tumor position monitoring and dynamic multileaf collimator tracking using a Siemens 160 MLC: Geometric and dosimetric accuracy of an integrated system. International Journal of Radiation Oncology* Biology* Physics 2011;79(2):579–87.
[12] Harris EJ, McNair HA, Evans PM. Feasibility of fully automated detection of fiducial markers implanted into the prostate using electronic portal imaging: A comparison of methods. International Journal of Radiation Oncology* Biology* Physics 2006;66(4):1263–70.
[13] Nederveen A, Lagendijk J, Hofman P. Detection of fiducial gold markers for automatic on-line megavoltage position verification using a marker extraction kernel (MEK). International Journal of Radiation Oncology* Biology* Physics 2000;47(5):1435–42.
[14] Meyer J, Richter A, Baier K, et al. Tracking moving objects with megavoltage portal imaging: A feasibility study. Medical Physics 2006;33:1275.
[15] Poulsen P, Fledelius W, Keall PJ, Weiss E, Lu J, Brackbill E, Hugo GD. A method for robust segmentation of arbitrarily shaped radiopaque structures in cone-beam CT projections. Medical Physics 2011;38(4):2151–6.
[16] Fast M, Teymurazyan A, Pang G, Oelfke U, Rowlands J. Finding an improved amorphous-silicon X-ray flat-panel detector configuration for the in-line geometry. Physics in medicine and biology 2013;58(7):2305.
[17] PerkinElmer, 6.10.4 sorting xrd 1640, XIS Reference Book X-Ray Imaging Software (2010) 78.
[18] Dagum L, Menon R. OpenMP: An industry standard API for shared-memory programming. Computational Science & Engineering, IEEE 1998;5(1):46–55.
[19] Poulsen PR, Cho B, Ruan D, Sawant A, Keall PJ. Dynamic multileaf collimator tracking of respiratory target motion based on a single kilovoltage imager during arc radiotherapy. International Journal of Radiation Oncology* Biology* Physics 2010;77(2):600–7.
[20] Dietrich L, Jetter S, Tücking T, et al. Linac-integrated 4d cone beam CT: First experimental results. Physics in medicine and biology 2006;51:2939.
[21] Balter JM, Wright JN, Newell LJ, et al. Accuracy of a wireless localization system for radiotherapy. International Journal of Radiation Oncology* Biology* Physics 2005;61(3):933–7.
[22] Lujan AE, Larsen EW, Balter JM, et al. A method for incorporating organ motion due to breathing into 3d dose calculations. Medical Physics 1999;26:715.
[23] Nill S, Unkelbach J, Dietrich L, et al. Online correction for respiratory motion: Evaluation of two different imaging geometries. Physics in medicine and biology 2005;50:4087.
[24] Richter A, Wilbert J, Baier K, Flentje M, Guckenberger M. Feasibility study for markerless tracking of lung tumors in stereotactic body radiotherapy. International Journal of Radiation Oncology* Biology* Physics 2010;78(2):618–27.
[25] Rottmann J, Aristophanous M, Chen A, Berbeco R, et al. A multi-region algorithm for markerless beam's-eye view lung tumor tracking. Physics in medicine and biology 2010;55(18):5585.
[26] Marchant T, Skalski A, Matuszewski B. Automatic tracking of implanted fiducial markers in cone beam CT projection images. Medical Physics 2012;39:1322.
[27] Poulsen PR, Cho B, Sawant A, Ruan D, Keall PJ. Detailed analysis of latencies in image-based dynamic MLC tracking. Medical Physics 2010;37(9):4998–5005.
[28] Cho B, Poulsen P, Sloutsky A, et al. First demonstration of combined kV/MV image-guided real-time dynamic multileaf-collimator target tracking. International Journal of Radiation Oncology* Biology* Physics 2009;74(3):859.
[29] Shirato H, Oita M, Fujita K, Watanabe Y, Miyasaka K. Feasibility of synchronization of real-time tumor-tracking radiotherapy and intensity-modulated radiotherapy from viewpoint of excessive dose from fluoroscopy. International Journal of Radiation Oncology*Biology*Physics 2004;60(1):335–41.

Author's personal copy

[30] Murphy M, Balter J, Balter S, et al. The management of imaging dose during image-guided radiotherapy: Report of the AAPM task group 75. Medical Physics 2007;34:4041.
[31] Krauss A, Fast M, Nill S, Oelfke U. Multileaf collimator tracking integrated with a novel X-ray imaging system and external surrogate monitoring. Physics in medicine and biology 2012;57(8): 2425.
[32] Ng J, Booth J, Poulsen P, Kuncic Z, Keall P. Estimation of effective imaging dose for kilovoltage intratreatment monitoring of the prostate position during cancer radiotherapy. Physics in medicine and biology 2013;58(17):5983.
[33] Furtado H, Gendrin C, Bloch C, et al. Real-time 2d/3d registration for tumor motion tracking during radiotherapy. SPIE Medical Imaging 2012;8314:831407.

Available online at www.sciencedirect.com
ScienceDirect